JOURNAL OF PROPULSION AND POWER
Vol. 15, No. 3, May–June 1999

Predicted Combined Effects of Purge Flow and Rotor-Casing Eccentricity on Ingress Heating

Zhou Guo* and David L. Rhode†
Texas A&M University, College Station, Texas 77843

The combined effect of purge/coolant flow rate and nonwhirling, rotor-casing radial eccentricity on the gas-turbine wheelspace cavity thermal environment was determined from a computational study. In this study, a series of Reynolds-averaged, Navier–Stokes numerical experiments was undertaken to obtain an improved understanding of mass ingress cavity heating. A recently developed and heavily tested three-scale k-ε turbulence model was utilized. The temperature, pressure, Mach number, and Reynolds number of a typical commercial gas-turbine engine were specified as appropriate for the mainstream, purge/coolant stream, and turbine wheel. At engine nominal conditions, no mass ingress (100% rim seal effectiveness) was found for the concentric-rotor case. However, for 50% rotor-casing eccentricity, large mass ingress and only 53% rim seal effectiveness were found. In addition, the minimum purge flow to prevent mass ingress increased markedly, i.e., from 8000 to 23,500 as the rotor eccentricity increased from 5 to 50%.

Nomenclature

C_w	=	purge/coolant volumetric flow rate parameter, $Q/(\phi R)$
$C_{w,\min}$	=	minimum volumetric flow rate parameter to prevent ingress, $Q_{\min}/(\phi R)$
e	=	seal eccentricity, i.e., displacement of rotor from casing centerline (percent of seal nominal clearance)
k	=	turbulent kinetic energy, $k^{(1)} + k^{(2)} + k^{(3)}$
$k^{(1)}$, $k^{(2)}$, $k^{(3)}$	=	partial turbulent kinetic energies
m_c	=	mass flow rate of coolant
$m_c/(m_c + \bar{m}_i)$	=	sealing effectiveness
m_{c0}	=	nominal value of mass flow rate of coolant
m_e	=	mass egress across x plane E–F, Fig. 1
m_i	=	mass ingress across x plane E–F, Fig. 1
Q	=	volumetric purge flow rate
R	=	radius of disk
$Re_{x,m}$	=	axial Reynolds number of mainstream, $2UH/\phi$
Re_θ	=	rotational Reynolds number of disk, $\Omega R^2/\phi$
R_i	=	radius of coolant inlet seal
T	=	temperature
T^*	=	normalized temperature, $(T - T_2)/(T_1 - T_2)$
U, V, W	=	mean velocities in x, r, θ directions
x, r, θ	=	axial, radial, and circumferential coordinates
x_i	=	spatial coordinate in tensor notation
ΔT^*	=	differential temperature, $2C_p(T_2 - T_1)/(\Omega R)^2$
ε	=	turbulent energy dissipation rate
$\varepsilon^{(1)}$, $\varepsilon^{(2)}$, $\varepsilon^{(3)}$	=	turbulence energy transfer rates

Subscripts

1	=	mainstream
2	=	cooling purge flow

Introduction

TO prevent gas-turbine wheelspace cavities from overheating, a purge/coolant flow rate (C_w) is injected into the wheelspace cavity, such as that of Fig. 1a, to purge the ingestion as well as to cool the disks. For this type of configuration, the coolant enters the cavity through a labyrinth seal at location 2, is centrifugally pumped by the rotor surface, and exits into the mainstream through the overlap rim seal. An unnecessarily large C_w is bled from the compressor because of the lack of understanding of the flow and thermal details. A complete rim seal stage analysis has never been attempted because of its complexity. However, numerous simplified subproblems have been investigated. For the external-flow-dominated regime, subproblem experimental studies of the effect of asymmetric mainstream pressures on ingress were conducted by Phadke and Owen,[1] who used tracer gas measurements to derive a correlation for the minimum purge flow to prevent ingress ($C_{w,\min}$). Similarly, Hamabe and Ishida[2] measured the ingress caused by mainstream pressure asymmetries resulting from a misaligned duct and proposed a correlation for $C_{w,\min}$. Fairly recently, Green and Turner[3] considered a more comprehensive subproblem that included the effects of the presence of guide vanes and blades, but excluded that of nonwhirling, rotor-casing eccentricity, which is illustrated in Fig. 1b. It was found that the presence of blades is important and gives a more nearly axisymmetric flow in the mainstream downstream of the rim seal.

Mainstream pressure asymmetries caused by various types of geometrical asymmetries[4] in the mainstream, including that resulting from rotor-causing eccentricity of the rim seal clearance, have been identified as important contributors to ingress. A particular lack of understanding in the external-flow-dominated regime involves the ingress increase caused by the nonwhirling, rotor-casing eccentricity. The nonwhirling eccentricity considered in the current study is caused by the accumulation of fabrication and/or assembly tolerances, as well as nonuniform thermal expansion. Eccentricity values in the 25–50% range are considered common.

There are several computational fluid dynamics (CFD) studies of the ingress subproblem in rotor–stator cavities, which include the mainstream, but exclude rotor-casing eccentricity. Those with a mainstream began with a laminar prediction by Vaughan and Turner.[5] A circumferential distribution of sinusoidally varying ingress–egress flow passing through a simple axial-clearance rim seal was found. More recently, Chew et al.[6] conducted a three-dimensional numerical study involving a simple axial-clearancerim seal using a simple mixing-length turbulence model. The mainstream had circumferential asymmetry in that the mainstream inlet boundary values were taken from the potential flow solution for flow through guide vanes. Comparison of measurements with numerical solutions gave generally reasonable agreement for seal effectiveness.

Received April 20, 1997; revision received Sept. 4, 1998; accepted for publication Oct. 13, 1998.

*Graduate Assistant, Turbomachinery Laboratories, Department of Mechanical Engineering; currently at EGS, Inc., 36,200 Plymouth Road, Livonia, MA 48150.

†Professor, Turbomachinery Laboratories, Department of Mechanical Engineering; currently at EGS, Inc., 36,200 Plymouth Road, Livonia, MA 48150. Member AIAA.

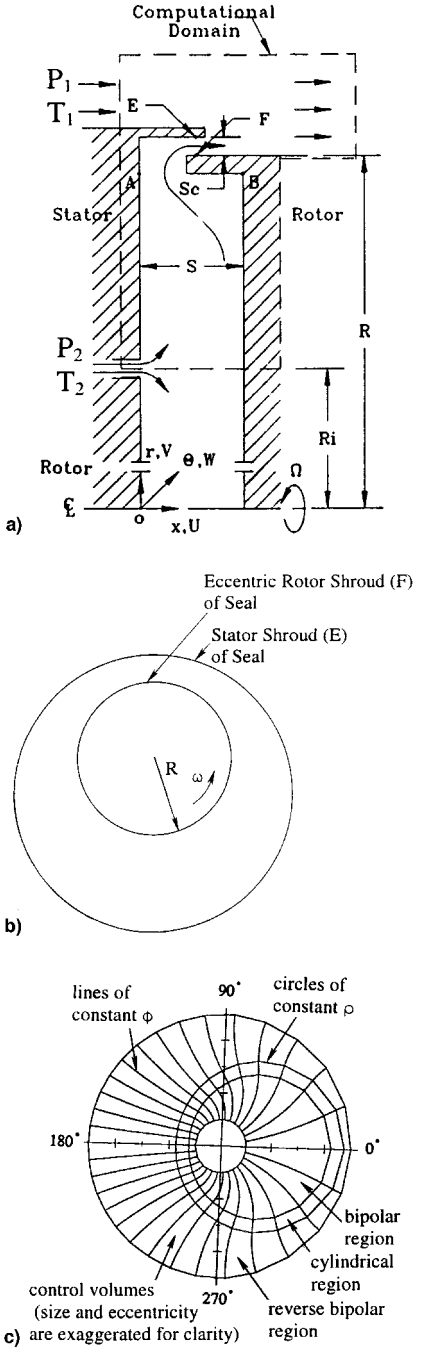

Fig. 1 Idealized configuration and computational domain: a) r–x plane view of the wheelspace cavity, b) exaggerated view of the r–θ plane showing the eccentric rotor, and c) arbitrary, exaggerated example showing the three types of grid region.

Lowry and Keeton[7] used a three-dimensional Navier–Stokes code, including the high Re number k-ε turbulence model, to predict the ingress heating in the unique rim seal cavity of the Space Shuttle turboprop, which has a circumferentially nonuniform turbine discharge pressure. The three, three-dimensional cases computed were 1) a base case that is geometrically axisymmetric with an asymmetric mainstream pressure distribution, 2) a rotor-casing eccentric rim seal with a correspondingly eccentric coolant inlet, and 3) a highly eccentric rim seal with a concentric coolant inlet. Although the Space Shuttle rim seal cavity involved a complicated geometry and different flow conditions from that of gas turbines, blade root temperatures were found to be quite sensitive to radial eccentricity.

For aircraft gas turbines, Guo et al.[8] examined eccentric rim seals where the purge air inlet, a circumferentially arranged series of orifices on the stator, was approximated as a circumferentially uniform slit. An earlier version of the present computer code was utilized, which, e.g., only had the standard k-ε model. Eccentricity effects on rim seal ingress and corresponding pressure drop were examined, but only for the engine normal purge flow. In contrast, the present paper gives the combined effect of C_w and eccentricity for the first time 1) on sealing effectiveness, 2) on purge flow to prevent ingress, $C_{w,\min}$, 3) as an approximate correlation for the dependence of $C_{w,\min}$ on eccentricity, and 4) on the wheelspace temperatures.

Objective

The objective is to obtain an enhanced understanding of the combined effect of purge/coolant flow and nonwhirling, rotor-casing eccentricity on the ingress heating of a generic wheelspace cavity of an aircraft engine. Specifically, items of primary interest include 1) the relationship and a simple correlation for the variation of $C_{w,\min}$ with eccentricity, 2) details of the rim seal gap recirculation zone for the ingress jet and for the egress jet, and 3) the increase of the blade root temperature with increasing eccentricity. The popular approach of studying the simplified subproblem, which excludes the nonuniformity imposed by the presence of vanes and blades in the mainstream, has been utilized. This subproblem approach isolates, for enhanced clarity, the circumferential pressure variation effect caused by rotor-casing eccentricity from that caused by the presence of vanes and blades. Adiabatic walls are specified to isolate ingress heating effects from wall heat convection effects, as frictional heating was found to be negligible at these conditions.

Computational Method

The fully compressible, elliptic, three-dimensional Reynolds-averaged Navier–Stokes code is based on the finite volume approach of discretizing the governing steady flow equations. The SIMPLER algorithm of Patankar[9] was employed using a system of four staggered grids for the primitive variables. The QUICK differencing scheme of Leonard[10] was incorporated for all convective terms in the momentum equations to reduce the false diffusion. The cyclic tri-diagonal matrix algorithm (CTDMA) was used to solve, in a segregated manner, each of the dependent variables. The option of a recently developed and extensively tested three-scale k-ε turbulence model was used, and is explained later. The iteration convergence criterion was that, for each governing equation, the sum of the local residual magnitudes, normalized by the appropriate inlet boundary quantities, must be < 0.001. The standard wall function for the resultant near-wall velocity and wall stress was used.

The steady governing equations used for the present predictions consist of the following continuity, momentum, and stagnation enthalpy (energy) equations, as well as the state equation and turbulence model equations. The first three of these equations are

$$\frac{\partial(\rho U_i)}{\partial x_i} = 0 \tag{1}$$

$$\frac{\partial(\rho U_i U_j)}{\partial x_i} = -\frac{\partial p}{\partial x_j} + \frac{\partial \mathfrak{v}_j}{\partial x_i} \tag{2}$$

$$\frac{\partial(\rho U_i H)}{\partial x_i} - \frac{\partial}{\partial x_j}\left(\Gamma_H \frac{\partial H}{\partial x_j}\right) = \frac{\partial}{\partial x_j}\left[U_l \mathfrak{v}_j - \Gamma_H \frac{\partial}{\partial x_j}\left(\frac{V^2}{2}\right)\right] \tag{3}$$

where ρ, U_i, and p are the time-averaged density, volume, and pressure, respectively. Here, Γ_H is defined as the ratio of the effective viscosity to effective Prandtl number, i.e.,

$$\Gamma_H = \mu_{\text{eff}}/Pr \tag{4}$$

The stator reference frame was utilized, and no-slip was specified on all rotor and stator surfaces via the wall functions (see the Domain and Boundary Conditions subsection). The equations were transformed as needed for general, i.e., any, orthogonal coordinates using Pope's[11] method. For additional details see Guo et al.[8]

Eccentric–Geometry Grids

The coolant enters the domain through a labyrinth seal rather than through a circumferentially arranged series of orifices. Thus, a nonwhirling, radially eccentric rotor gives a circumferentially varying radial clearance for the coolant inlet labyrinth seal and also the rim seal (see Fig. 1b). The r–θ cross section of the domain is divided into grid regions of three types, each of which is shown for an arbitrary example of exaggerated eccentricity and grid coarseness (Fig. 1c). A bipolar-coordinate grid[12] will easily give a body-fitted grid line along each boundary of this region. Thus, a cylindrical coordinate grid is used in cylindrical regions, and a bipolar-coordinate (or reverse bipolar-coordinate) grid is used for regions with eccentricity. In constructing the overall composite grid, the grid lines on opposing sides of a grid region interface are carefully patched together so that a grid line of constant χ is in alignment across the interface.

The grids were constructed starting at the coolant inlet clearance (eccentric) region, where bipolar coordinates are utilized. Next, for the outer surface of the rotor shroud to be concentric with the rotor surface of the coolant inlet seal, a transition is made to a reverse-bipolar-coordinate grid region (of equal but opposite displacement from the first bipolar region). Next is a transition to a cylindrical-coordinate grid, which extends radially outward to the outer surface of the rotor shroud. The next region contains a bipolar-coordinate grid, like that of the coolant inlet, with grid lines coinciding with the sealing surfaces of the rim seal. Finally, the outer boundary of the domain is made concentric with the inner surface of the stator shroud by using a cylindrical-coordinate grid to cover that portion of the domain.

Bipolar coordinates may be related to Cartesian coordinates by the following transformation:

$$x = \frac{-a\sinh(\rho)}{\cosh(\rho) - \cos(\chi)} \tag{5}$$

$$y = \frac{a\sin(\chi)}{\cosh(\rho) - \cos(\chi)} \tag{6}$$

where ρ denotes the radius of a circle, and χ denotes the position along that circle.

The current production grid is highly nonuniform with $44 \times 44 \times 25$ lines in the x, r, and θ directions. In the final test, it was determined that the preceding grid gives a sensibly grid-independent solution in that a 50% increase in the number of grid points ($54 \times 54 \times 25$) gives a deviation from the preceding grid of only 0.2 and 0.9% for the cavity-averaged temperature and rim seal effectiveness, respectively. The grid has no skewness because of the orthogonality of the bipolar and cylindrical coordinate systems. Grid stretching factors of up to 15% were utilized with cell aspect rations generally between 0.25 and 4.0. The grid-independence testing was conducted for the case of 25% eccentricity and $C_w = 7200$.

Turbulence Modeling

One deficiency of the standard k-ε model is the use of a single length scale and time scale to represent the entire range of eddy size for the energy-containing (non-Kolmogorov) eddies. Different sizes of turbulent eddies show a substantially different rate of development. Thus, each eddy size should be characterized by its inherent length and time scales, which allows that eddy size to respond at its own rate to sudden changes in the mean flow. A second deficiency of the standard k-ε model is the use of merely physical/dimensional arguments to obtain the algebraic form of the source/sink terms of the ε equation. Both of these deficiencies have been overcome in the present investigation, by using a more sophisticated type of k-ε turbulence model, the three-scale k-ε model of Guo and Rhode.[13] Specifically, there is distinct modeling for each of the three eddy-size groups, i.e., for each of the large, medium, and small ranges of energy-containing eddy size. Production dominates for the large-size eddies, whereas the energy cascade dominates for the medium- and the small-size eddies. The three-scale model, along with its two-scale variant by Ko and Rhode,[14] is quite unique in that it is derived from the dynamic equation for the anisotropic turbulence energy spectrum.

For each of the three eddy sizes, the partial turbulence energies $k^{(1)}$, $k^{(2)}$, or $k^{(3)}$ are computed from the transport equation derived for each. These are given as

$$\frac{Dk^{(1)}}{Dt} - \frac{\partial}{\partial x_i}\left[\frac{\nu_{\text{eff}}}{\sigma_k}\frac{\partial k^{(1)}}{\partial x_i}\right] = P - \varepsilon^{(1)} \tag{7}$$

$$\frac{Dk^{(2)}}{Dt} - \frac{\partial}{\partial x_i}\left[\frac{\nu_{\text{eff}}}{\sigma_k}\frac{\partial k^{(2)}}{\partial x_i}\right] = \varepsilon^{(1)} - \varepsilon^{(2)} \tag{8}$$

$$\frac{Dk^{(3)}}{Dt} - \frac{\partial}{\partial x_i}\left[\frac{\nu_{\text{eff}}}{\sigma_k}\frac{\partial k^{(3)}}{\partial x_i}\right] = \varepsilon^{(2)} - \varepsilon^{(3)} \tag{9}$$

where $k^{(1)}$, $k^{(2)}$, and $k^{(3)}$ are the large-, intermediate-, and smaller-eddy partial turbulence energies that are found in the production, the larger-eddy cascade, and smaller-eddy cascade portions of the spectrum, respectively. Note that the turbulence kinetic energy $k = k^{(1)} + k^{(2)} + k^{(3)}$ and that the energy dissipation ε is equal to $\varepsilon^{(3)}$, whereas $\varepsilon^{(2)}$ and $\varepsilon^{(3)}$ are interpreted as energy transfer rates.

The governing equation for the energy transfer rate leaving each of the three zones $\varepsilon^{(1)}$, $\varepsilon^{(2)}$, and $\varepsilon^{(3)}$ is given as

$$\frac{D\varepsilon^{(1)}}{Dt} - \frac{\partial}{\partial x_i}\left[\frac{\nu_{\text{eff}}}{\sigma_\varepsilon}\frac{\partial \varepsilon^{(1)}}{\partial x_i}\right] = C^{(1)}\frac{\varepsilon^{(1)}P}{k^{(1)}} - C_2^{(1)}\frac{\varepsilon^{(1)^2}}{k^{(1)}} \tag{10}$$

$$\frac{D\varepsilon^{(2)}}{Dt} - \frac{\partial}{\partial x_i}\left[\frac{\nu_{\text{eff}}}{\sigma_\varepsilon}\frac{\partial \varepsilon^{(2)}}{\partial x_i}\right] = -C_1^{(2)}\frac{\varepsilon^{(2)^2}}{k^{(2)}} + C_2^{(2)}\frac{\varepsilon^{(1)}\varepsilon^{(2)}}{k^{(2)}} + C_3^{(2)}\frac{P\varepsilon^{(2)}}{k^{(2)}} - C_4^{(2)}\frac{P\varepsilon^{(2)}}{k^{(1)}} + C_5^{(2)}\frac{\varepsilon^{(1)}\varepsilon^{(2)}}{k^{(1)}} \tag{11}$$

$$\frac{D\varepsilon^{(3)}}{Dt} - \frac{\partial}{\partial x_i}\left[\frac{\nu_{\text{eff}}}{\sigma_\varepsilon}\frac{\partial \varepsilon^{(3)}}{\partial x_i}\right] = -C_1^{(3)}\frac{P\varepsilon^{(3)}}{k^{(1)}} - C_2^{(3)}\frac{P\varepsilon^{(3)}}{k^{(2)}} + C_3^{(3)}\frac{P\varepsilon^{(3)}}{k^{(3)}} + C_4^{(3)}\frac{\varepsilon^{(1)}\varepsilon^{(3)}}{k^{(1)}} + C_5^{(3)}\frac{\varepsilon^{(1)}\varepsilon^{(3)}}{k^{(2)}} - C_6^{(3)}\frac{\varepsilon^{(1)}\varepsilon^{(3)}}{k^{(3)}} + C_7^{(3)}\frac{\varepsilon^{(2)}\varepsilon^{(3)}}{k^{(2)}} + C_8^{(3)}\frac{\varepsilon^{(2)}\varepsilon^{(3)}}{k^{(3)}} - C_9^{(3)}\frac{\varepsilon^{(3)^2}}{k^{(3)}} \tag{12}$$

The derivation of the model coefficients follows that of Ko and Rhode.[14] Other details along with the coefficient values are found in Guo and Rhode.[13] The expression for the turbulent eddy viscosity is given as

$$\nu_t = \frac{C_\mu\left[k^{(1)} + k^{(2)} + k^{(3)}\right]^2}{\varepsilon^{(3)}} \tag{13}$$

where $\varepsilon^{(3)}$ simply results from the algebra of the derivation.[14]

Three-Scale Model Testing

The idealized axial-clearance rim seal without a mainstream[1] constitutes an important test case for assessing the three-scale model. The operating conditions are 1) coolant flow coefficient, $C_w = 2950$; 2) seal clearance ratio, $G_c = 0.01$; and 3) cavity gap ratio, $G = 0.1$. It is shown in Fig. 2 that predictions from the three-scale model and the single-scale (standard) model are in close agreement with measurements at moderate rotational Reynolds numbers. However, at high rotational Reynolds numbers, the improvement of the three-scale model over the single-scale model is clearly seen, although a discrepancy still exists. The lower rotational Reynolds number cases measured are not considered here because of a concern that a low Re model may be required for them.

Model testing using the rotor–stator cases of Daily et al.[15] was also conducted. Because it was found that the three-scale model gives the same solution as the two-scale model for such a rotor–stator cavity case in particular, the three-scale model is being designated as multiscale for this case. Numerous computations were made for Re_θ,

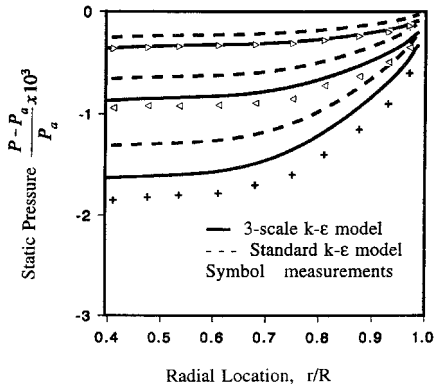

Fig. 2 Radial distribution of mean static pressure for the rotor–stator cavity using the three-scale model (C_w = 2950, G_c = 0.01, G = 0.1). $Re_\theta/10^6$: 0.6 (▷), 0.8 (◁), and 1.0 (+).

ranging from 2×10^6 to 9.5×10^6, and a volumetric flow rate C_w ranging from 1500 to 13,000. The multiscale wall shear stress was considerably improved over that of the single-scale model, yielding a friction moment coefficient that was ~4% rather than 25% underpredicted over the entire Re_θ range.

The three-scale model has been tested over a wide range of popular noncavity test cases as well. For example, for the wake recirculation zone length behind a disk, measured by Carmody,[16] the three-scale model gave an 11.6% underprediction vs 25.6% underprediction for the single-scale model. In addition, the three-scale model overpredicted the measured spreading rate of the axisymmetric free-jet of Capp[17] by 16%, rather than 23% for the single-scale model. Similarly, the three-scale model underpredicted the spreading rate of the swirling freejet of Pratte and Keffer[18] by 1.6% vs ~10.2% for the single-scale model. Further, the three-scale model overpredicted the skin friction coefficient for the boundary layer with an adverse pressure gradient of Samuel and Joubert[19] by 16.1%, whereas the single-scale model underpredicted it by 19.7%. For the defying case of the recirculation zone length of the annular freejet, measured by Durao and Whitelaw,[20] the multiscale model and also the single-scale model gave a 21% underprediction.

In summary, the improvement of the three-scale model is attributed to more physics being included in the derivation.

Domain and Boundary Conditions

Figure 1a shows the idealized cavity configuration and computational domain. The radial clearance and axial overlap of the rim seal shrouds were 1.9 and 2.0 mm, respectively. Other important dimensions of the generalized cavity considered are 1) radius of the rotor, $R = 0.3078$ m; 2) inlet radial width of the mainstream passage, $H/R = 0.026$; 3) axial width of the cavity, $s/R = 0.0612$; 4) radial location of the cavity inlet, $R/R = 0.904$; and 5) radial width of the cavity inlet, $a/R = 0.00725$.

Essentially, all studies of mainstream ingress into such rotor–stator cavities contain an inherent uncertainty concerning how far away from the region of interest the domain boundaries must be located. No definitive, detailed measurements (or computations) of the necessary mainstream boundary condition values a distance upstream and downstream of the nonuniform rim seal clearance are available. Moreover, the mainstream axial velocity is drastically higher (in the present case by a factor of 160) than that of the ingress and egress. Thus, the effect of the mainstream is extremely slight and localized (as shown in subsequent results), occurring only over the short axial length of the rim seal. Thus, in keeping with previous authors, the computational domain extends axially a short distance upstream and downstream from the rim seal. For the current generalized subproblem, approximating the mainstream duct as a straight passage, rather than a diverging one, is reasonable for obtaining an enhanced first-order insight. This is because the effect of the diverging mainstream duct is generally counterbalanced by the increasing boundary-layer displacement thickness, which results from the significant mainstream swirl velocity.

Numerical iteration convergence, when including the entire radial height of the mainstream, proved difficult (stiff governing equations), and could be alleviated by reducing the number of grid lines. Thus it was desirable to reduce the radial height of the mainstream within the domain to reduce the number of grid lines without loss of accuracy. Because the mainstream axial velocity is dramatically higher than that of the ingress and egress flow, only a narrow, radially inner portion of the mainstream interacts with the rim seal (as shown later). Thus, the radial extent of the mainstream included in the domain was reduced. Because the ingress velocity is drastically weaker than the mainstream velocity, zero radial velocity at the radially outer boundary within the mainstream is a reasonable boundary condition. Further, because 1) the swirl velocity is not high in the present cases (near 50% of the axial velocity), and 2) the mainstream outer boundary values are unknown, it was decided to utilize the boundary condition sometimes used for swirling boundary layers. That is, zero radial velocity and zero radial derivative of all other quantities were specified at the radially outer boundary, which lies in the mainstream (see Fig. 1a). A series of numerical experiments, each having a different mainstream radial extent, was carefully examined in selecting a final domain radial extent that would reduce the required number of grid lines. For example, it was found that an increase of the domain height of 50%, over that of the currently used domain, gave a deviation of cavity-averaged temperature and seal effectiveness of only 0.01 and 1.3%, respectively.

Similarly, a series of numerical experiments was conducted in which the domain exit for each case was moved farther downstream. Using the zero axial gradient outflow boundary condition, this series allowed determination of an outlet location required to avoid the outlet boundary being located too close to the recirculation zone downstream of the stator shroud.

The mainstream inlet boundary values were chosen as those leaving an upstream stator vane. Specifically, the inlet values for axial and tangential velocities, as well as enthalpy, temperature, and pressure, were obtained from generic commercial aircraft engine values, supplied by Ivey,[‡] as 1) axial Reynolds number in the main pass, $Re_{x,m} = 3.12 \times 10^5$; 2) rotational Reynolds number of the rotor, $Re_\theta = 7.62 \times 10^6$; 3) cooling flow rate, $C_w = 3600$, 7200, and 14,400; 4) differential pressure, $\Delta P^* = -0.01$; 5) differential temperature, $\Delta T^* = -4.6$; and 6) swirl ratio at the main pass domain inlet, $W/U = \tan(\pi/12)$. The $Re_{x,m}$ represents a mainstream axial velocity of 360 m/s. As a close approximation, the mainstream inlet radial velocity was set to zero because the mainstream mass flow is higher than the ingress/egress flow by a factor of 160.

Along rotor and stator wall boundaries, the well-known wall function[21] was used for both velocity components tangential to the wall, as well as for evaluating the turbulence production term in the $k^{(1)}$ equation. Freestream boundary conditions were assumed at the radially outer boundary of the domain, which lies in the mainstream.

Results and Discussion

Although the mainstream pressure is higher than that within the wheelspace cavity, the predictions obtained herein for concentric rotor cases (not shown for brevity) show the expected absence of mass ingress with a very slight heat ingress into the wheelspace cavity. The slight heat ingress is a result of a very slight net axial turbulent heat diffusion from the mainstream through the rim seal. Rotor centrifugal pumping cooperates with the coolant purge flow to provide sufficient discouragement to mass ingress. However, the circumferentially varying radial clearance asymmetry shown in Fig. 1b typically occurs at the rim seal (discussed earlier), as well as at the purge air inlet labyrinth seal. It was found that such rim seal eccentricity dramatically increases the mainstream heat ingress via a large mass ingress from the mainstream into the cavity, the turbulent axial diffusion remaining almost constant.

A gap recirculation zone (GRZ) forms downstream of the rim seal radial clearance overlap step height, as shown by the velocity vectors in Fig. 3a. Specifically, the circumferentially varying rim

[‡]Ivey, P., personal communication, Cranfield Inst. of Technology, UK, 1990.

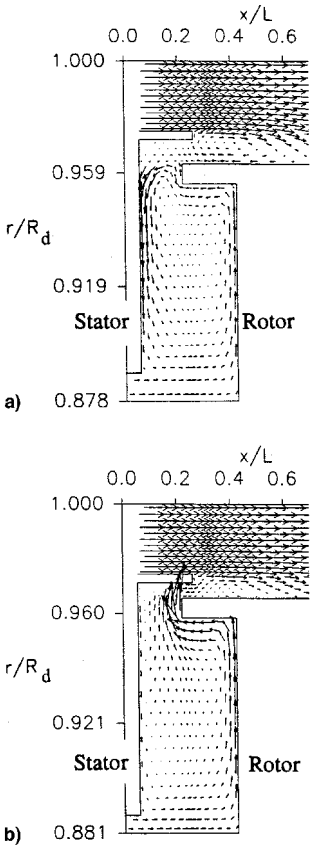

Fig. 3 Velocity vectors for 50% eccentricity at the θ = a) 28.8-deg and b) 260-deg plane (mainstream vectors have been scaled down by a factor of 3.75 for clarity).

seal radial clearance causes the expected circumferential variation in the axial length of the recirculating wake downstream of the radial clearance. A corresponding rim seal pressure asymmetry occurs in accordance with the local variation of the balance of pressure, inertia, shear, and centrifugal forces. The result for all combinations of eccentricity and purge flow considered here is that a circumferentially distributed peak of mainstream mass ingress enters the rim seal near the circumferential location of largest clearance, which is at the cylindrical coordinate plane of $\theta = 0$ deg. Subsequently, it exits the rim seal to enter the cavity at approximately $\theta = 25$ deg (displaced in the rotation direction) because of the transit time required for a particle to pass through the rim seal.

The velocity vectors for the r–x plane of approximately the maximum mass ingress ($\theta = 28.8$ deg) and for 50% rotor eccentricity are shown in Fig. 3a. The vectors in the mainstream are scaled down by a factor of 3.75 for graphical clarity. Observe here that the GRZ separates from, and reattaches to, the trailing edge (location D) of the stator shroud shown in Fig. 1a. As mentioned earlier, because this r–x plane has almost the largest radial clearance, it has almost the largest axial length of the GRZ, which Fig. 3a shows is about $x/L = 0.55$, where L is an arbitrary length. Observe further in Fig. 3a that a very small portion of the mainstream passes downstream along the GRZ, makes a 180-deg turn, and then flows upstream along the radially outer surface of the rotor shroud where it enters the rim seal. Note that the mass ingress entering the rim seal occupies less than half of the local radial clearance. The flow pattern of the circumferentially distributed mass ingress jet, described earlier, occurs for the nominal $C_w = 7200$ over a circumferential range of 145 deg, for $C_w = 3600$ over a range of 155 deg, and for $C_w = 14{,}400$ over a range of 110 deg.

Observe further in Fig. 3a that the expected overall cavity recirculation zone is found, which is driven in the counterclockwise direction by the purge inlet flow, the rotor centrifugal pumping, and the mass ingress. Also note that the hot mass ingress impinges immediately on the stator wall near $r/R_d = 0.96$, without significant mixing with the cooler cavity fluid. Next, the ingress flows radially inward on a helical path along the stator wall, mixing somewhat with the cavity fluid. Most of the purge fluid, which enters through a labyrinth seal of corresponding rotor displacement, occurs as a somewhat similar jet of circumferentially varying strength, where the circumferential peak at the cavity inlet is located near $\theta = 0$ deg. After a degree of mixing with the purge inlet jet, the mainstream ingress jet then proceeds along a helical path radially outward along the rotor, where the near-wall radial velocity is maintained at a fairly high value by centrifugal pumping.

Outside of the mass ingress circumferential zone of the rim seal is the mass egress zone, which exhibits the flow pattern shown in Fig. 3b (the mainstream vectors are scaled down by a factor of 3.75). This plot shows the plane $\theta = 260$ deg for 50% eccentricity, which is near the plane of maximum egress (actually occurring at $\theta = 300$ deg for $C_w = 3600, 7200$, and 14,400). Observe in this figure that the egress flows axially in the mainstream direction through the rim seal, occupying the entire local radial clearance. Upon exiting the rim seal, it immediately flows radially outward near location D (Fig. 1a), where it undergoes transverse, i.e., radial, turbulent mixing with the mainstream as it is axially accelerated by the mainstream. Note that, as the egress jet is accelerated, it drives a slightly different GRZ than that of the ingress jet. This egress GRZ separates from and reattaches to the outer surface of the rotor shroud as indicated by the velocity vectors in Fig. 3b. Further, because of the smaller local radial clearance than that of the ingress jet, this egress GRZ is much shorter in axial extent, beginning at $x/L = 0.35$ and ending at $x/L = 0.45$. In addition, compared with the $\theta = 28.8$-deg overall cavity flow pattern (Fig. 3a), the radially outward portion of the cavity exhibits a much larger radial velocity across most of the axial width of the cavity, with much less velocity inward along the stator wall.

Seal Ingress

The sealing effectiveness $[m_c/(m_c + \bar{m}_i)]$ is evaluated via circumferential integration of the mass ingress m_i. The previously unknown effect of eccentricity on the variation of sealing effectiveness with purge flow, C_w, is shown in Fig. 4. At the engine nominal C_w of 7200, the effectiveness is ~96% for 5% eccentricity. Further, note that increases of eccentricity give increased ingress for each C_w, so that seal performance is drastically reduced for large eccentricities. For example, at the engine nominal C_w value, the effectiveness decreases from 96 to 53% as the eccentricity increases from 5 to 50%. There is a wide variety of aircraft engines for which rotor eccentricity in the range of 25–50% is believed to be common. The performance penalty resulting from rotor eccentricity arises from an increased C_w required to compensate for the increased mass ingress.

The previously unknown variation of the minimum coolant necessary to prevent ingress, $C_{w,\min}$, with eccentricity is shown in Fig. 5. It can be seen that $C_{w,\min}$ increases markedly and almost linearly with increasing eccentricity. Observe that an eccentricity increase from 5 to only 50% increases $C_{w,\min}$ from ~8000 to 23,500. A correlation for the $C_{w,\min}$ variation with eccentricity at the temperatures, pressures, Mach numbers, and Re numbers, which are typical of

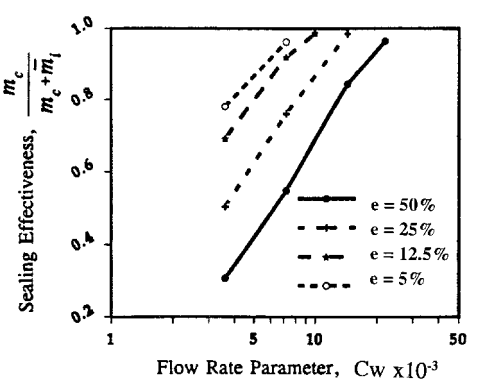

Fig. 4 Effects of C_w on the sealing effectiveness.

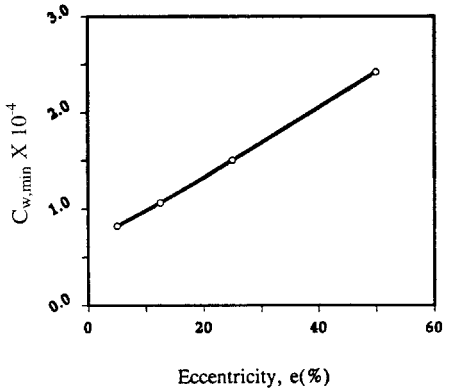

Fig. 5 Variation of the minimum cooling airflow rate $C_{w,\min}$ with eccentricity.

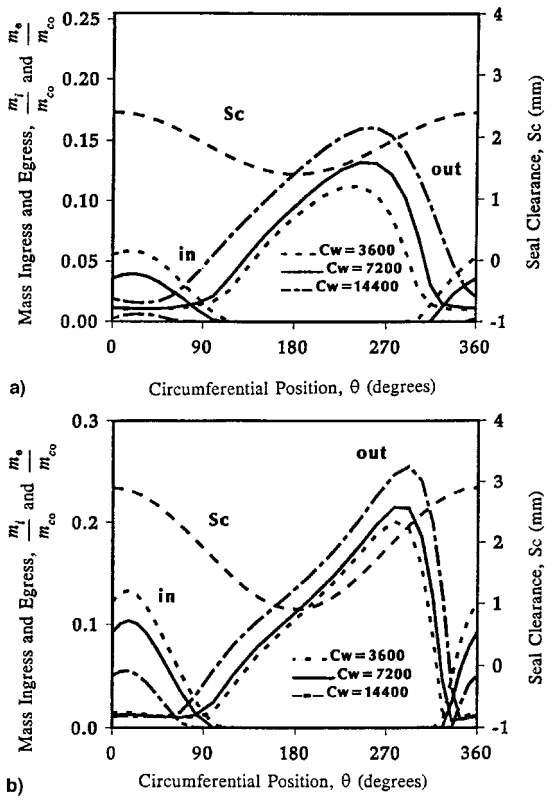

Fig. 6 Effects of C_w on circumferential variation of the mass ingress and mass egress as well as seal clearance for a) 25 and b) 50% eccentricity.

many commercial aircraft engines (see the Domain and Boundary Conditions subsection), is given as

$$C_{w,\min} = 0.658e^2 + 320.1e + 6552.9 \tag{14}$$

where seal eccentricity e is in percent of the seal nominal clearance, i.e., $e = 50$ for 50%. Application of this correlation at significantly different operating conditions would require a corresponding uncertainty on a case-by-case basis, as no measurements are available for comparison. Very large computing resources would be required to obtain a broad-based correlation involving the Re number.

Figures 6a and 6b show the effects of C_w on the circumferential distributions of the mass ingress and egress for eccentricities of 25 and 50%, respectively. The circumferentially varying rim seal radial clearance S_c is also shown here for reference. The mass ingress and egress are nondimensionalized by the typical engine nominal mass flow rate of cooling air, m_{c0}. The results show that the ingress phenomenon occurs for all three C_w values considered, although

Table 1 Hottest location and its temperature

C_w	Surface	$T^*_{\max}$	r/R	θ, deg
	a) 50% eccentricity			
3,600	Rotor	0.502	0.981	256
	Stator	1	0.989	43
7,200	Rotor	0.404	0.982	242
	Stator	0.99	0.989	43
14,400	Rotor	0.311	0.981	242
	Stator	0.8	0.989	72
	b) 25% eccentricity			
3,600	Rotor	0.265	0.981	272
	Stator	0.783	0.989	58
7,200	Rotor	0.178	0.981	272
	Stator	0.56	0.989	58
14,400	Rotor	0.154	0.981	301
	Stator	0.141	0.978	73
	c) 12.5% eccentricity			
3,600	Rotor	0.154	0.981	301.8
	Stator	0.29	0.989	72
7,200	Rotor	0.128	0.981	316.3
	Stator	0.146	0.968	101.5
14,400	Rotor	0.121	0.981	345.4
	Stator	0.117	0.96	130.1

doubling the nominal coolant flow to $C_w = 14{,}400$ at 50% eccentricity does not eliminate it. The circumferential location of maximum ingress and egress velocity is fairly independent of C_w as well as eccentricity. Specifically, the location of maximum ingress and egress is ~25 and 300 deg, respectively, which is almost identical to the corresponding values found previously by Guo et al.[8] for the orifice type of purge inlet and nominal C_w. To conserve mass in the cavity, the egress must decrease with a decreasing coolant flow. However, Figs. 6a and 6b show that the egress level at $C_w = 3600$ is close to that at $C_w = 7200$. This is because of counterbalancing effect involving the facts that 1) the egress flow is the sum of the coolant and ingress flows and 2) a low coolant situation gives high ingress. Thus, the increased ingress at $C_w = 3600$, compared with 7200, results in nearly the same egress.

Cavity-Averaged Temperature

The cavity-averaged temperature, which is the average over all axial, radial, and circumferential locations, indicates total heating via ingress and disk frictional heating because adiabatic walls are used. The previously unknown effect of C_w at various eccentricities on cavity-averaged temperature is shown in Fig. 7. Note the large increases of cavity-averaged temperature for any C_w values caused by rim seal ingress as the eccentricity surpasses a threshold value (about 5%). Also observe that, as C_w decreases below the engine nominal value of 7200, the averaged temperature increases more rapidly, especially for the higher eccentricity cases shown. Similarly, it was found in case B of Lowry and Keeton[7] that the temperature in the cavity, for a rim seal with 28% eccentricity, increased 42°C (75°F) over that of the concentric case.

Adiabatic Surface Temperature

Even for the present case, where ingress is the sole source of heat, the maximum rotor temperature is located near the blade root. This location is not surprising because it is the farthest location on the rotor from the coolant inlet. The cooling of the blade root is important because of thermal reliability concerns. The temperature and position of the highest temperature location on the rotor and on the stator for each C_w considered are given in Table 1 for the three C_w values and for the three eccentricity values. Examining the highest rotor temperature for the nominal C_w and eccentricities of 12.5, 25, and 50%, one finds dimensionless temperatures of 0.128, 0.178, and 0.404, respectively. This variation is a reflection of the increasing rate of cavity temperature rise with increasing eccentricity, as seen in Fig. 7. Also, note that at 50% eccentricity and C_w values of 3600, 7200, and 14,400, the maximum rotor temperatures are 0.502, 0.404, and 0.311, respectively. These temperatures indicate

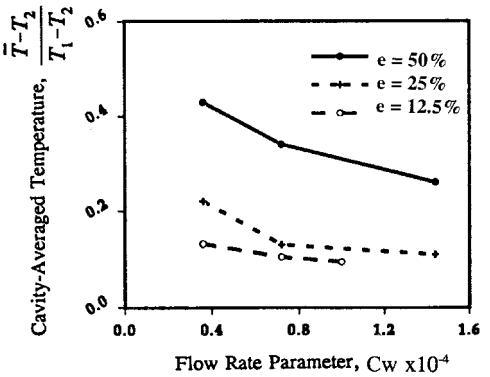

Fig. 7 Variation of the cavity-averaged temperature with C_w.

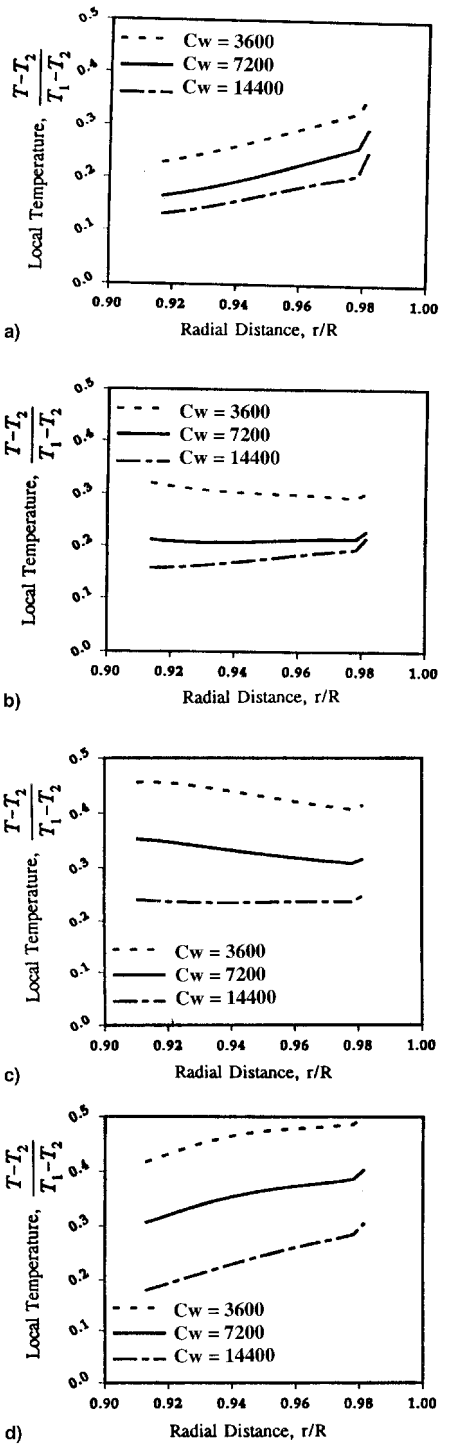

Fig. 8 Effect of C_w on radial distributions of the dimensionless temperature on the rotor for 50% eccentricity at θ = a) 0, b) 86.4, c) 172.8, and d) 259.2 deg.

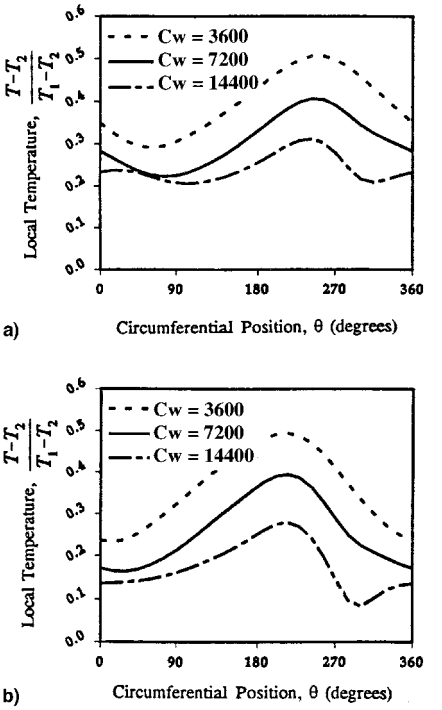

Fig. 9 Effect of C_w on circumferential distributions of the dimensionless temperature on the rotor for 50% eccentricity at r/R = a) 0.98 and b) 0.92.

the large increase of purge/coolant required to significantly reduce the maximum rotor temperature below that of the nominal C_w. In addition, it is interesting to observe the effect of the helical path of the mainstream ingress jet in Table 1 (part a), e.g., where the highest temperature on the rotor for 50% eccentricity is generally found near 250 deg, whereas that on the stator is generally near 50 deg.

For 50% eccentricity, Figs. 8a–8d show the effects of C_w on the radial distributions of the rotor adiabatic temperature at various circumferential locations. The radial increase of temperature for $C_w = 3600$, because of increased mass ingress, is clearly seen. Specifically, the rotor temperatures $\theta = 0$ and 259.2 deg increase with radial position and reach a maximum at the blade root/retainer, whereas those at $\theta = 86.4$ and 172.8 deg remain almost constant. These distributions result from the interaction of the circumferentially nonuniform coolant jet and mass ingress jet. Further, the effects of C_w on the circumferential distribution of the rotor temperature at the blade root/retainer ($r/R = 0.98$) and at the inner portion of the domain ($r/R = 0.92$) are shown in Figs. 9a and 9b for 50% eccentricity. At low C_w, the circumferential variation of rotor temperature is almost sinusoidal, whereas the complicated mixing of the ingress and purge/coolant streams at high C_w gives a nonsinusoidal distribution.

Summary

A three-dimensional Navier–Stokes computer program was used with engine nominal temperatures, pressures, Mach numbers, and Reynolds numbers for a displaced-rotor wheelspace cavity exhibiting an eccentric coolant inlet seal as well as an eccentric rim seal. Wall convection heating was eliminated by using adiabatic walls. Previously unknown findings include the following:

1) The concentric-rotor situation at engine nominal C_w gives no mass ingress with very slight turbulent heat diffusion ingress. However, as the rotor eccentricity increases from 5 to 50%, the rim seal effectiveness decreases from 96 to 53% because of the considerable mainstream ingress jet.

2) $C_{w,\min}$ increases substantially with rotor eccentricity in an almost linear fashion. For example, an eccentricity increase from 5 to 50% increases $C_{w,\min}$ from ~8000 to 23,500.

3) An approximate correlation for estimating $C_{w,\min}$ as a function of eccentricity is given, although caution should be used in applying it for substantially different conditions.

4) Specific details of the gap recirculation zone for the ingress and egress jets are examined.

5) The circumferential location of maximum ingress velocity, $\theta = 25$ deg, is independent of C_w as well as eccentricity. The circumferential location of maximum egress velocity, approximately $\theta = 300$ deg, is fairly insensitive to C_w as well as to rotor eccentricity.

6) At 50% eccentricity, mainstream ingress persists in the presence of large increases of C_w, even if C_w is doubled from the engine nominal value of 7200 to 14,400.

7) As C_w decreases below the typical engine nominal value of 7200, the cavity-averaged temperature increases more sharply with further decreases of C_w.

8) For 50% eccentricity, the highest blade root dimensionless temperature for $C_w = 3600$ is extremely high at 0.502, which is 24% higher than that for $C_w = 7200$.

Acknowledgment

The authors are grateful to the Supercomputer Center at the Texas A&M University for a grant of Cray Y-MP computer time.

References

[1]Phadke, U. P., and Owen, J. M., "Aerodynamic Aspects of the Sealing of Gas-Turbine Rotor-Stator Systems, Part 2: The Performance of Simple Seals in a Quasi-Axisymmetric External Flow," *International Journal of Heat and Fluid Flow*, Vol. 9, No. 2, 1988, pp. 106–112.

[2]Hamabe, K., and Ishida, K., "Rim Seal Experiments and Analysis of a Rotor-Stator System with Nonaxisymmetric Main Flow," American Society of Mechanical Engineers, Paper 92-GT-160, June 1992.

[3]Green, T., and Turner, A. B., "Ingestion into the Upstream Wheelspace of an Axial Turbine Stage," *Journal of Turbomachinery*, Vol. 116, 1994, pp. 327–332.

[4]Johnson, B. V., Mack, G. J., Paolillo, R. E., and Daniels, W. A., "Turbine Rim Seal Gas Path Flow Ingestion Mechanisms," AIAA Paper 94-2703, June 1994.

[5]Vaughan, C. M., and Turner, A. B., "Numerical Prediction of Axisymmetric Flow in a Rotor-Stator System with an External Mainstream Flow," *Proceedings of the 5th International Conference on Numerical Methods in Laminar and Turbulent Flows* (Swansea, Wales, UK), 1987.

[6]Chew, J. W., Green, T., and Turner, A. B., "Rim Sealing of Rotor-Stator Wheelspaces in the Presence of External Flow," American Society of Mechanical Engineers, Paper 94-GT-126, June 1994.

[7]Lowry, S. A., and Keeton, L. W., "Space Shuttle Main Engine High Pressure Fuel Pump Aft Platform Seal Cavity Flow Analysis," NASA TP-2685, 1987.

[8]Guo, Z., Rhode, D. L., and Davis, F. M., "Computed Eccentricity Effects on Turbine Rim Seals at Engine Conditions with a Mainstream," *Journal of Turbomachinery*, Vol. 118, 1996, pp. 143–152.

[9]Patankar, S. V., *Numerical Heat Transfer and Fluid Flow*, McGraw–Hill, New York, 1980.

[10]Leonard, B. P., "A Stable and Accurate Convective Modeling Procedure Based on Quadratic Upstream Interpolation," *Computer Methods in Applied Mechanics and Engineering*, Vol. 19, 1979, pp. 59–98.

[11]Pope, S. B., "The Calculation of Turbulent Recirculation Flows in General Coordinates," *Journal of Computational Physics*, Vol. 26, 1978, pp. 197–217.

[12]Kamal, M. M., "Separation in the Flow Between Eccentric Rotating Cylinders," *Journal of Basic Engineering*, Vol. 88, 1966, pp. 717–724.

[13]Guo, Z., and Rhode, D. L., "Assessment of Two- and Three-Scale k-ε Models for Rotating Cavity Flows," *Journal of Turbomachinery*, Vol. 18, 1996, pp. 826–834.

[14]Ko, S. H., and Rhode, D. L., "Derivation and Testing of a New Multi-Scale k-ε Turbulence Model," AIAA Paper 90-0243, Jan. 1990.

[15]Daily, J. W., Ernst, W. D., and Asbedian, V. V., "Enclosed Rotating Disks with Superposed Throughflow," Hydrodynamics Lab., Massachusetts Inst. of Technology Rept. 64, Cambridge, MA, 1964.

[16]Carmody, T., "Establishment of the Wake Behind a Disk," *Journal of Basic Engineering*, Vol. 86, 1964, pp. 869–882.

[17]Capp, S. P., "Experimental Investigation of the Turbulent Axisymmetric Jet," Ph.D. Dissertation, State Univ. of New York, Buffalo, NY, 1983.

[18]Pratte, B. D., and Keffer, J. F., "The Swirling Turbulent Jet," *Journal of Basic Engineering*, Vol. 94, 1972, pp. 739–748.

[19]Samuel, A. E., and Joubert, P. N., "A Boundary-Layer Developing in an Increasingly Adverse Pressure Gradient," *Journal of Fluid Mechanics*, Vol. 66, 1974, pp. 481–505.

[20]Durao, D. F. G., and Whitelaw, J. H., "Velocity Characteristics of the Flow in the Near Wake of a Disk," *Journal of Fluid Mechanics*, Vol. 85, Pt. 2, 1978, pp. 369–385.

[21]Launder, B. E., and Spalding, D. B., "The Numerical Computation of Turbulent Flows," *Computer Methods in Applied Mechanics and Engineering*, Vol. 3, 1974, pp. 269–289.